Los Alamos NATIONAL LABORATORY EST.1943

LA-UR-15-28803 (Accepted Manuscript)

Multiple loss processes of relativistic electrons outside the heart of outer radiation belt during a storm sudden commencement

Yu, J.
Li, L. Y.
Cao, J. B.
Yuan, Z. G.
Reeves, Geoffrey D.
Baker, D. N.
Blake, J. B.
Kletzing, C.
Spence, H. E.

Provided by the author(s) and the Los Alamos National Laboratory (2017-10-17).

To be published in: Journal of Geophysical Research: Space Physics

DOI to publisher's version: 10.1002/2015JA021460

Permalink to record: http://permalink.lanl.gov/object/view?what=info:lanl-repo/lareport/LA-UR-15-28803

Disclaimer:
Approved for public release. Los Alamos National Laboratory, an affirmative action/equal opportunity employer, is operated by the Los Alamos National Security, LLC for the National Nuclear Security Administration of the U.S. Department of Energy under contract DE-AC52-06NA25396. Los Alamos National Laboratory strongly supports academic freedom and a researcher's right to publish; as an institution, however, the Laboratory does not endorse the viewpoint of a publication or guarantee its technical correctness.

RESEARCH LIBRARY

Multiple loss processes of relativistic electrons outside the heart of outer radiation belt during a storm sudden commencement

J. Yu[1], L.Y. Li[1], J. B. Cao[1], Z. G. Yuan[2], G. D. Reeves[3], D. N. Baker[4], J. B. Blake[5], H. Spence[6]

[1]School of Astronautics, Beihang University, Beijing, China

[2]School of Electronic Information, Wuhan University, Wuhan, China

[3]Space Sciences and Applications Group, Los Alamos National Laboratory, Los Alamos, New Mexico, USA

[4]Laboratory for Atmospheric and Space Physics, University of Colorado Boulder, Boulder, Colorado, USA

[5]The Aerospace Corporation, Los Anglees, California, USA

[6]Institue for the Study of Earth, Oceans, and Space, University of New Hampshire, Durham, New Hampshire, USA

By examining the compression-induced changes in the electron phase space density and pitch angle distribution observed by two satellites of Van Allen Probes (RBSP-A/B), we find that the relativistic electrons (> 2MeV) outside the heart of outer radiation belt ($L^* \geq 5$) undergo multiple losses during a storm sudden commencement (SSC). The relativistic electron loss mainly occurs in the field-aligned direction (pitch angle $\alpha < 30°$ or $>150°$), and the flux decay of the field-aligned

electrons is independent of the spatial location variations of the two satellites. However, the relativistic electrons in the pitch angle range of 30°-150° increase (decrease) with the decreasing (increasing) geocentric distance ($|\Delta L|< 0.25$) of the RBSP-B (RBSP-A) location, and the electron fluxes in the quasi-perpendicular direction display energy-dispersive oscillations in the Pc5 period range (2 - 10min). The relativistic electron loss is confirmed by the decrease of electron phase space density at high-L shell after the magnetospheric compressions, and their loss is associated with the intense plasmaspheric hiss, electromagnetic ion cyclotron (EMIC) waves, relativistic electron precipitation (observed by POES/NOAA satellites at 850km) and magnetic field fluctuations in the Pc5 band. The intense EMIC waves and whistler-mode hiss jointly cause the rapidly pitch angle scattering loss of the relativistic electrons within 10 hours. Moreover, the Pc5 ULF waves also lead to the slowly outward radial diffusion of the relativistic electrons in the high-L region with a negative electron phase space density gradient.

1. Introduction

Relativistic electrons (> 0.5MeV) in the Earth's outer radiation belt are often changed by intense solar wind disturbances and/or geomagnetic activity. The increased solar wind dynamic pressure can result in the enhancement or loss of the relativistic electrons in different regions of the outer radiation belt [*Li et al*., 1993; 2003; *Lee et al*., 2005; *Li et al*., 2013a]. Moreover, the relativistic electron flux usually decreases during main phase of a storm (*Dst*< -30nT) [*Reeves et al.,* 2003; *Li*

45 *et al*., 2009]. The main phase depletion of the relativistic electrons can be attributed to
46 the *Dst* effect [*Kim and Chan*, 1997], outward radial diffusion [*Shprits et al.*, 2006;
47 *Turner et al*., 2012], magnetopause shadowing [*Kim et al.*, 2008; *Saito et al*., 2010;
48 *Matsumura et al.*, 2011; *Hudson et al.*, 2014] and/or wave-particle interactions [*Li et*
49 *al.*, 2007; *Summers et al.*, 2007; *Xiao et al.*, 2009; *Thorne*, 2010; *Su et al.*, 2012; *Tu et*
50 *al.*, 2013; *Ni et al.*, 2013].

51 The *Dst* effect is a adiabatic response of the relativistic electron flux to the
52 decrease of magnetic field during the main phase of a storm [*Kim and Chan*, 1997].
53 Associated with the decrease of magnetic field, the charged particle's drift shells
54 expand outward to conserve their third adiabatic invariant (i.e., magnetic flux
55 $\Phi = \oint \vec{B} \cdot d\vec{A}$), and meanwhile the outward moving particles undergo adiabatic
56 decelerations when their first and second adiabatic invariants are constant. Moreover,
57 the magnetopause shadowing and the outward radial diffusion can also lead to the
58 decrease of the outer zone relativistic electrons [*Shprits et al.*, 2006; *Loto'aniu et al.*,
59 2010; *Turner et al*., 2012]. Since the energetic particles whose equatorial pitch angle
60 is 90^o have a largest drift orbit radius on the dayside, those particles around 90^o are
61 more easily lost to the dayside magnetopause [*Hudson et al.*, 2014]. Although the
62 electromagnetic ion cyclotron (EMIC) waves and the plasmaspheric hiss have also
63 been suggested to be responsible for the relativistic electron loss during the main
64 phase of a storm [*Summers and Thorne*, 2003; *Li et al.*, 2007; *Summers et al.*, 2007;
65 *Thorne*, 2010], there is no directly observational evidence to indicate that the
66 wave-induced electron loss begins at a storm sudden commencement (SSC).

By examining the compression-induced changes in the relativistic electron phase space density and pitch angle distribution observed by two satellites of Van Allen Probes (RBSP-A/B), we find that the relativistic electrons outside the heart of outer radiation belt ($L^* \geq 5$) undergo multiple losses during a SSC when various waves are amplified prior to the storm main phase. The relevant data is introduced in the section 2. The observations are presented in the section 3. The discussions are performed in the sections 4 and 5, and the conclusions are summarized in the section 6.

2. Data Source

In this paper, solar wind dynamic pressure (P_d) and geomagnetic field horizontal component (H_{SYM}) come from OMNI database in the Coordinated Data Analysis Web. Energetic particle fluxes and wave data are observed by two satellites of Van Allen Probes (RBSP-A and RBSP-B). The relevant instruments include the Energetic Particle, Composition, and Thermal Plasma (ECT) suite [*Spence et al.*, 2013], the Relativistic Electron Proton Telescope (REPT) [*Baker et al.,* 2013] and the Electric and Magnetic field Instrument Suite and Integrated Science (EMFISIS) [*Kletzing et al.,* 2013].

In addition, EMIC waves are obtained through the band filtering of magnetic field data measured by the GOES satellite and Canadian Array for Realtime Investigations of Magnetic Activity (CARSIMA) [*Mann et al.*, 2008]. The precipitating energetic particles (0^o pitch angle) are measured by the Medium Energy Proton and Electron Detector (MEPED) aboard the Polar Orbiting Environmental Satellites (POES) of

National Oceanic and Atmospheric Administration (NOAA) [*Evans and Greer*, 2000].

3. Relativistic Electron Loss During A SSC

Figure 1 displays the solar wind dynamic pressure (P_d), position (R_{MP}) of the subsolar magnetopause, horizontal component (H_{SYM}) of geomagnetic field, K_p index, energy spectrum of relativistic electrons and location (L value) of RBSP-B satellite during the interval from 17:00 UT on 30 October to 05:00 UT on 01 November 2012. R_{MP} is calculated through an empirical model of the magnetopause position [*Shue et al.*, 1998]. The 1-minute averaged K_p is available at http://www.rbsp-ect.lanl.gov/data_pub/QinDenton/. Before ~ 15:38 UT on 31 October 2012 (on the left of vertical dashed line), geomagnetic activity is very weak (H_{SYM}~ 0-10nT and $K_p \leq 1$) during a small and stable solar wind dynamic pressure (P_d ~ 1nPa, and $|\Delta P_d|$<~0.5nPa), and the flux of relativistic electrons (~ 2.0- 6.0MeV) is larger than 10 (#/cm^2.s.sr.MeV) in the region of $L > 2$.

After ~ 15:38 UT on 31 October (on the right of vertical dashed line), the dynamic pressure enhancement ($\Delta P_d > 7$nPa) results in the earthward displacement of the subsolar magnetopause (ΔR_{MP}~ -2R_E) and the severe compression of the Earth's magnetosphere ($\Delta H_{SYM} > 20$nT). However, K_p is still small ($1 < K_p \leq 3$) during the magnetospheric compressions. Interestingly, the magnetospheric compressions lead to the flux decay of the relativistic electrons in the high-L region (L> 5) after ~20:00 UT on 31 October. The significant electron depletion is displayed in the red rectangle in

Figure 1c.

In order to exclude the adiabatic electron flux changes, we calculated the electron phase space density in the space of three adiabatic invariants (μ, K, L^*). μ, K and L^* are the first, second and third adiabatic invariants, respectively. For the relativistic electrons of a specified energy (E), their three adiabatic invariants and phase space density (f) are expressed as [*Kim et al.*, 1997; *Chen et al.*, 2007; *Morley et al.*, 2013; *Reeves et al.*, 2013]:

$$\mu = \frac{E\left(E + 2E_0\right)}{2BE_0}\sin^2\alpha \tag{1}$$

$$K = \int_{s_s}^{s_n}\sqrt{B_m - B\left(s\right)}ds \tag{2}$$

$$L^* = \frac{2\pi M}{\Phi R_E} \tag{3}$$

$$f\left(\mu, K, L^*\right) = 3.325\times10^{-11}\frac{j\left(E, \alpha, r\right)}{E\left(E + 2E_0\right)} \tag{4}$$

Here, E_0 and α are the electron rest energy and pitch angle, respectively. B and B_m are magnetic field strengths at the observed location and at the mirror point, respectively. s is path length of electrons bouncing along the field line, $\Phi = \oint \vec{B}\cdot d\vec{A}$ is the magnetic flux within a drift shell of energetic particles, M is the Earth's magnetic moment, and R_E is the Earth's radius.

Three adiabatic invariants (μ, K, L^*) and phase space density (f) of the relativistic electrons are obtained from the RBSP-B/REPT electron data and the TS04D (aka TS05) magnetic field model [*Tsyganenko and Sitnov*, 2005]. Figures 2a and 2b show the radial (L^*) profile of electron phase space density (Mu=3000MeV/G, K=0.115, $0.285G^{1/2}/R_E$) in the TS04D model in different intervals. The different times

correspond to the start time of each pass. Before the dynamic pressure enhancement (before ~ 15:38 UT on 31 October), the phase space density of relativistic electrons at different pitch angles (i.e., different K) is large in the entire outer zone (L^* ~ 3.4- 6). After the dynamic pressure enhancement (after ~ 15:38 UT), the electron phase space density decreases remarkably outside the heart of outer radiation belt ($L^* \geq 4.6$), indicating that some relativistic electrons at high-L shell are really lost during the SSC, and the electron loss at higher-L shell is larger than that at lower-L shell.

The electron phase space density radial profile in TS04D model is similar to that in T89 model [*Tsyganenko*, 1989] (not shown here), suggesting that the influence of different magnetic field models is small in the dipolar field region (L~ 1- 6.5). Figures 2c and 2d show the observed value (colored asterisks) and model value of the magnetic field (B) and the occurrence probability of magnetic field relative errors ($(B_{observed}-B_{model})/B_{observed}$) in this event. The model value (B_{model}) of the magnetic field can approximately agree with its observed value ($B_{observed}$) at the same L^*, and the averaged and maximum relative errors are ~ 4% and ~15% during this event. According to the error estimation by *Reeves et al.* [2013], the uncertainty in the electron phase space density, caused by the magnetic field error of ~4%-15%, is less than a factor of 1.5-3.0.

The maximum relative error of the magnetic field appears at the time of the IP shock impact. Figures 3a and 3b show the observed (black solid line) and model (black dash line) magnetic fields (B_{tot}) and their relative error (red dot line). The relative error is less than 10% before the magnetospheric compressions (before

15:38UT), but it increases to 12%- 15% during the IP shock impact (15:38 - 16:00UT). Thereafter the relative error decreases to a level less than 12%. Therefore, the influence of the magnetic field models on the electron phase space density is very small most of the time, except for the interval 15:38 - 16:00UT.

Associated with the decrease of electron phase space density, pitch angle distribution of the relativistic electrons is also changed during the SSC. Figures 3c-n display the spin-averaged fluxes (all pitch angles) and pitch angle distributions of different-energy relativistic electrons (2.0- 4.5MeV) observed by the two satellites during the interval 15:30-16:30UT on 31 October. Before the dynamic pressure enhancement (before ~ 15:38UT), the magnetic field (B_{tot}) is less than 180nT, and the electron fluxes and pitch angle spectra are quite stable in paths of the two satellites. Although the quasi-perpendicular distributed electrons (α~ 30°-150°) are dominant population, there are also considerable field-aligned electrons (α< 30° and >150°) before the dynamic pressure enhancement (indicated by the left part of the vertical dashed lines in Figures 3e-n).

After the dynamic pressure enhancement (after ~15:38 UT on 31 October), the magnetic field increases suddenly to a level above 180nT (Figures 3a, h). The sudden magnetospheric compressions result in the energy-dispersive oscillations (period ~ 2-8 min) in the spin-averaged electron fluxes and pitch angle spectra (indicated by the right part of the vertical dashed lines in Figures 3e-n). Interestingly, the relativistic electron fluxes in the pitch angle range of 30°- 150° decrease with the increasing geocentric distance (ΔL~ 0.15) of the outbound RBSP-A satellite, but increase with

176 the decreasing geocentric distance ($\Delta L\sim$ - 0.24) of the inbound RBSP-B satellite.
177 Unlike the quasi-perpendicular distributed electrons, the electron fluxes in the
178 field-aligned ($\alpha< 30°$ and $> 150°$) direction decrease remarkably at the two satellite
179 locations ($L> 5.7$) after the dynamic pressure enhancement (i.e. after ~15:38 UT on 31
180 October). The field-aligned flux decay is consistent with the decreased electron phase
181 space density at high-L shell (see Figure 2), indicating that a portion of the relativistic
182 electrons is really removed from the outer radiation belt during the SSC.
183
184 **4. Loss Processes of Relativistic Electrons**
185 During the SSC, the relativistic electron fluxes in the quasi-perpendicular
186 direction are still larger than those in the field-aligned direction. The large
187 quasi-perpendicular fluxes are inconsistent with the magnetopause shadowing loss
188 mainly at large pitch angles [*Hudson et al*., 2014]. On the contrary, the field-aligned
189 electron loss, observed by Van Allen Probes, is similar to the pitch angle scattering
190 loss caused by high-frequency plasma waves (whistler-mode hiss and EMIC waves)
191 [*Li et al*., 2013b; *Usanova et al.*, 2014]. Meanwhile, the electron flux oscillations in
192 Pc5 band also suggest that the relativistic electrons probably undergo the outward
193 radial diffusion in the high-L region with a negative electron phase space density
194 gradient.
195
196 **4.1. Electron Pitch Angle Scatterings by the EMIC Waves and Hiss**
197 During the SSC, EMIC waves and plasmaspheric hiss are observed by some

198 ground stations (MCMU, RABB, FSMI, OXFO, SOD, IVA and KIL) and satellites
199 (RBSP-A, RBSP-B, GOES-13 and GOES-14) at high-L shell. Figure 4 shows the
200 equatorial projection of the wave-measured locations during the interval 15:30-16:30
201 UT on 31 October. The intense wave activities are observed just at the electron drift
202 shells outside the heart of outer radiation belt (> $5R_E$). Figure 5 displays a portion of
203 the EMIC waves in the space (GOES-13) and on the ground (MCMU, RABB and
204 FSMI). Before the dynamic pressure enhancement (before ~ 15:38UT), power
205 spectral density (PSD) of the EMIC waves is less than 10^{-2} nT^2/Hz in the Pc1-2 band
206 (0.1-0.5Hz). After the dynamic pressure enhancement (after ~ 15:38UT), the EMIC
207 waves (0.1-0.5Hz) are simultaneously amplified (PSD≥ $0.1nT^2/Hz$) in the space and
208 on the ground (indicated on the right of vertical dashed line in Figure 5). Multipoint
209 measurements indicate that the EMIC waves can be amplified in a wide MLT range
210 (MLT~ 9- 23:00) at high-L shell (> $5R_E$) during the SSC. By testing the polarization
211 ellipticity (ε> 0 denotes right-hand polarized, and ε= 0 denotes linear polarized, and
212 ε< 0 denotes left-hand polarized, and ε= ±1 denotes circular polarized [*Santolík et al.*,
213 2003]), we found that the compression-amplified EMIC waves are mainly left-hand
214 polarized (ε < -0.3).

215 Although the RBSP-A and RBSP-B satellites only measured very weak EMIC
216 waves on the dawnside (PSD< $0.1nT^2/Hz$), they observed intense plasmaspheric hiss.
217 Figure 6 shows the plasma density, wave intensity (PSD), normal angle (WNA) and
218 polarization ellipticity at the RBSP-B location during this event. Before 22:00 UT on
219 31 October, RBSP-B satellite was moving inside the plasmasphere where the plasma

density is higher than 50cm^{-3} in the region of L< 5.5. During the late compression stage (22:00UT/31/10- 02:00UT/01/11), the satellite moved temporarily into a low-density trough where the plasma density is less than 50cm^{-3} in the high-L region (L> 5.5), owing to the shrinkage of the plasmasphere. After 02:00UT/01/11, it entered again the high-density plasmasphere.

Inside the high-density plasmasphere (density > 50cm^{-3}, and L< 5.5), the satellite measured the intense plasmaspheric hiss (PSD $\geq 10^{-6}$ nT^2/Hz) in the whistler-mode frequency range (f~ 0.01-0.1f_{ce}, f_{ce} is the electron gyrofrequency). The whistler-mode hiss (f~ 0.01- 0.5$f$ce) are quasi-parallel propagating (WNA< 30°) and right-hand polarized (ε > 0.5). However, there are only very weak whistler-mode chorus waves (PSD~ 10^{-8} nT^2/Hz in the frequency of 0.1< f < 0.5f_{ce}) in the low-density trough (density> 50cm^{-3}, and L> 5.5) during late phase of the event (22:00UT/31/10-02:00UT/01/11).

Comparing Figure 1c with Figure 6, it can be found that there is about one day lag between the hiss emissions and the electron flux dropouts. This indicates that the electron pitch angle scattering by hiss is very slow, and the electron loss should be small if there is only the hiss. Therefore, the intense EMIC waves are required for the large loss of relativistic electrons within the observed interval. Moreover, the role of the brief and weak chorus waves is negligible during the wave-particle interactions.

In a cold plasma containing multiple ions (H^+, He^+, O^+), the dispersion relation of the parallel-propagating whistler-mode (s= 1) or EMIC waves (s= -1) can be normalized as [*Stix*, 1992]:

$$k_s^2 = \omega_s^2 + \rho\omega_s\left(\frac{1}{s-\omega_s} - \frac{\varepsilon\eta_1}{\omega_s + s\varepsilon} - \frac{\varepsilon\eta_2}{4\omega_s + s\varepsilon} - \frac{\varepsilon\eta_3}{16\omega_s + s\varepsilon}\right) \quad (5)$$

where the normalized wave number $k_s = ck/|\Omega_{ce}|$ (c is the light speed, k_s is the parallel wave number, and Ω_{ce} is angular frequency of the electron gyration motion), and the normalized wave frequency $\omega_s = \omega/|\Omega_{ce}|$ (ω is the wave frequency), and the plasma frequency $\omega_{pe} = (4\pi N_0 e^2/m_e)^{1/2}$ (N_0 and m_e are the electron number density and mass, respectively). $\rho = \omega_{pe}^2/\Omega_{ce}^2$, $\varepsilon = m_e/m_p$ (m_p is the proton mass), $\eta_1 = N_1/N_0$, $\eta_2 = N_2/N_0$, $\eta_3 = N_3/N_0$ (N_1, N_2 and N_3 are the hydrogen, helium and oxygen number density, respectively).

The power spectral density (B_ω) of the observed waves is fitted as a Gaussian frequency distribution, and

$$B_\omega^2 = \begin{cases} A^2 \exp\left[-(\omega-\omega_m)^2/\delta\omega^2\right] & for \quad \omega_{lc} < \omega < \omega_{uc} \\ 0 & otherwise \end{cases} \quad (6)$$

$$A^2 = \frac{B_t^2}{\delta\omega}\frac{2}{\sqrt{\pi}}\left[erf\left(\frac{\omega_{uc}-\omega_m}{\delta\omega}\right) + erf\left(\frac{\omega_m-\omega_{lc}}{\delta\omega}\right)\right]^{-1} \quad (7)$$

where ω_m is the wave frequency at PSD peak, and $\delta\omega$ is bandwidth. B_t is the wave magnetic field magnitude.

The parallel-propagating whistler-mode and EMIC waves can resonate with electrons when the gyroresonance condition is satisfied:

$$\gamma\omega_{sr} - k_{sr}p_r\cos\alpha = s \quad (8)$$

where ω_{sr} is the resonant wave frequency, and k_{sr} is the resonant wave number, and α is the electron pitch angle ($\tan\alpha = v_\perp/v_\parallel$, $v_\perp$ and $v_\parallel$ are the electron velocities parallel and perpendicular to the background magnetic field), the normalized momentum of electron $p_r = p/m_e c$, and the relativistic factor $\gamma = (1+p_r^2)^{1/2}$.

For the small-amplitude resonant waves, the temporal evolution of the resonant electron pitch angle distributions is determined by the quasi-liner diffusion (Fokker-Planck) equation [*Lyons and Williams*, 1984]:

$$\frac{\partial f}{\partial t} = \frac{1}{G}\frac{\partial}{\partial \alpha_0}\left(G\hat{D}_{\alpha\alpha}\frac{\partial f}{\partial \alpha_0}\right) - \frac{f}{\tau} \quad (9)$$

where $G = T_B(\alpha_0)\sin\alpha_0\cos\alpha_0$ (α_0 is the equatorial pitch angle and $T_B(\alpha_0) \approx 1.30\text{-}0.56\sin\alpha_0$), τ is the loss time (it equals a quarter of the bounced period inside the loss cone and infinity outside the loss cone), and $\hat{D}_{\alpha\alpha}$ is the bounce-averaged pitch angle diffusion coefficient [*Summers*, 2005; *Xiao et al*., 2009]:

$$\hat{D}_{\alpha\alpha} = \frac{1}{T_B}\int_0^{\lambda_m} D_{\alpha\alpha}\frac{\cos\alpha}{\cos^2\alpha_0}\cos^7\lambda d\lambda \quad (10)$$

$$D_{\alpha\alpha} = |\Omega_{ce}|^2\left(\frac{1}{\gamma^2}I_0 - 2I_1\frac{1}{\gamma p_s}\cos\alpha + I_2\frac{1}{p_s^2}\cos^2\alpha\right) \quad (11)$$

$$I_n = \pi\sum_{k_{sr}}\frac{B_{\omega r}^2}{B_0^2}\left(\frac{\omega_{sr}}{k_{sr}}\right)^n\left|1 - \cos\alpha\frac{p_s}{\gamma}\frac{dk_s}{d\omega_s}\right|^{-1}_{k_s = k_{sr}} \quad (12)$$

where λ_m is the mirror point latitude, n is 0, 1 and 2. B_0 is the background magnetic field strength. $B_{\omega r}^2$ (in unit of nT^2/Hz) is the wave PSD at a resonant frequency ω_{sr}.

During the wave-driven pitch angle scatterings, the loss of the scattered particles is limited by the particle number in the loss cone. When the pitch angle diffusion of the particles is faster than their loss to the atmosphere, a large number of particles are rapidly scattered into the loss cone so that their pitch angle distributions become isotropic [*Shprits et al*., 2009]. Thereafter, the pitch angle scattering can reach an equilibrium state in the absence of the particle phase space density gradient (i.e., $\partial f/\partial\alpha_0 = 0$), as indicated by Equation 9. The upper limit (D_{SD}) of the electron pitch

angle diffusion coefficient is a function of the electron energy (E) and L shell [*Summers and Thorne*, 2003], and

$$D_{SD} \approx \frac{9.66}{L^4}\left[\frac{4L}{4L-3}\right]^{1/2}\frac{\left[E(E+2)\right]^{1/2}}{(E+1)} \quad (13)$$

Using the observed wave parameters (Hiss: B_t= 102pT, λ_m= 40°, $\omega_{lc}/2\pi$= 30Hz, $\omega_{uc}/2\pi$= 200Hz, $\omega_m/2\pi$= 95Hz, $\delta\omega/2\pi$= 42Hz; EMIC waves: B_t= 2.55nT, λ_m= 15°, ω_{lc}= 1.675Ω_{O+}, ω_{uc}= 3.908Ω_{O+}, ω_m= 2.702Ω_{O+}, $\delta\omega$= 0.502Ω_{O+}. Ω_{O+} is the oxygen gyrofrequency), we modeled the electron pitch angle scatterings caused by the hiss and EMIC waves. The initial and boundary conditions are expressed as: $f(\alpha_0, t=0)= f_0\sin^q\alpha_0$ (f_0 and q can be obtained via fitting the observational data), and $f(\alpha_0=0)= 0$, and $\partial f/\partial\alpha_0(\alpha_0=90)= 0$ [*Xiao et al.*, 2009]. The MLT distribution percentages of the hiss and EMIC waves are assumed to be ~5% and 1% at L= 5.2, and the ambient ions consist of ~70% hydrogen (H^+), 20% helium (He^+) and 10% oxygen (O^+) [*Meredith et al.*, 2003; *Summers et al.*, 2003; 2007]. In addition, we also adopt the plasma density model established by *Sheely et al.* [2001].

Figure 7 displays the bounced-drift-averaged pitch-angle diffusion coefficients $<D_{\alpha\alpha}>$ of different-energy electrons (2.0MeV, 2.85MeV, 3.6MeV) and their pitch angle evolutions from the initial distribution (blue curve) to the scattered distribution (red curve). The strong diffusion limit (D_{SD}) is plotted as the dashed lines in Figures 7a-c. The EMIC waves mainly scatter the relativistic electrons at small pitch angles ($\alpha< 70°$, indicated by blue lines in Figures 7a-c), whereas the hiss can scatter the relativistic electrons at large pitch angles ($\alpha > 70°$, indicated by red lines in Figures 7a-c). The combined scatterings by two types of the waves can approximately

reproduce the observed electron pitch angle evolution from the initial distribution (blue dots) to the scattered distribution (red dots) (see Figure 7d-e). The electron flux decreases after the wave actions, indicating that the observed hiss and EMIC waves are able to effectively scatter the relativistic electrons into the loss cone during the SSC.

During the SSC, the relativistic electron precipitation is observed by low-orbit satellites. The vertical shades in Figure 8 display the particle precipitation (30-80keV protons and > 1MeV electrons) observed by the POES METOP-2 and NOAA-19/16 satellites at ~ 850km (where L> 4.6). The brief enhancements of the energetic proton and relativistic electron fluxes at 0° pitch angle are usually considered as the particle precipitation signals caused by the EMIC waves [*Yuan et al*., 2013; *Usanova et al*., 2014; *Wang et al*., 2014]. Owing to the satellite orbit limit, the particle precipitation signals are mainly observed around the low-altitude foot points of the electron loss regions on the duskside and nightside (L~ 4.6- 5.6 and MLT~ 20:36- 23:00). The wide particle precipitation regions suggest that the EMIC waves are amplified in a wider MLT range than the available observed points. This is consistent with the previous statistical results that the EMIC waves can be excited at the most MLTs in the region of L~ 4- 10 [*Clausen et al*., 2011; *Min et al*., 2012; *Carson et al*., 2013].

4.2.Outward Radial Diffusions Driven By ULF Waves

Although our observations and simulations indicate that the combined pitch angle scatterings by the hiss and EMIC waves can cause the significant loss of the

relativistic electrons, this does not exclude the possibility of the electron outward radial diffusion in the high-L region with a negative electron phase space density gradient. In fact, a negative radial gradient of the relativistic electron phase space density is produced in the high-L (L^*> 5) region after 10:50UT on 31 October (see Figure 2), and the spin-averaged electron fluxes and pitch angle spectra display energy-dispersive oscillations in the Pc5 period range (see Figure 4). The quasi-periodic electron flux oscillations during this event have been testified to be the ULF drift resonance [*Mann et al.*, 2013; *Claudepierre et al.*, 2013]. In principle, the strong ULF waves can drive the electron outward radial diffusions in the high-L region ($L^* \geq 5$) with a negative electron phase space density gradient [*Shprits et al.*, 2006; *Turner et al.*, 2012].

Based on the analysis method of ULF waves [*Liu et al.*, 2009], we rotated the RBSP-measured magnetic field vector into a Mean-Field-Aligned (MFA) coordinate system. Figures 9a-f display the magnetic field PSDs in the radial, azimuthal and field-aligned directions. The PSDs of the Pc5 ULF waves (~ 2- 6 mHz) increase remarkably after the magnetospheric compressions (after 15:38 UT on 31 October). The particle's radial diffusion coefficient (D_{LL}^B) is a function of the PSD (P_m^B) of the compressional magnetic field perturbation [*Fei et al.*, 2006; *Loto'aniu et al.*, 2010; *Ozeke et al.*, 2014], and

$$D_{LL}^B = \frac{\mu^2}{8q^2\gamma^2 B_s^2 R_E^4} \cdot L^4 \cdot \sum_m m^2 P_m^B \qquad (14)$$

where μ is the first adiabatic invariant, and q is the electron charge, γ is the relativistic Lorentz factor, B_s is the equatorial magnetic field on the Earth's surface, R_E is the

Earth's radius, L is the Mcllwain parameter, m is the azimuthal wave mode number. P_m^B is a total power of the compressional magnetic field perturbation in the frequency range of f~ 2-6mHz. Since the ULF wave periods ($1/f$ ~ 2.7- 8.3min in Figure 9) are comparable to the drift periods ($\Omega_e/2\pi$) of the relativistic electrons (> 0.5 MeV) in the region of L~ 5 - 6, the relativistic electrons can resonate with the Pc5 ULF waves through m=1 (i.e., the wave angular frequency $\omega \sim \Omega_e$). This point is confirmed by the energy-dispersive electron flux oscillations in the Pc5 period range.

Besides the magnetic field fluctuation, the electric field fluctuation can also play a more important role in the radial diffusion of the radiation belt particles [*Tu et al*., 2012; *Ozeke et al*., 2014]. Regretfully, the azimuthal electric field component that determines the radial diffusion coefficient (D_{LL}^E) cannot be obtained at the dawnside satellite locations, as expounded by *Claudepierre et al*. [2013]. The empirical radial diffusion coefficients are a function of K_p index [*Ozeke et al.*, 2014]:

$$D_{LL}^B = 6.62\times10^{-13} L^8 10^{-0.0327L^2+0.625L-0.0108K_p^2+0.449K_p} \quad (15)$$

$$D_{LL}^E = 2.16\times10^{-8} L^6 10^{0.217L+0.461K_p} \quad (16)$$

The total radial diffusion rate $D_{LL} = D^B{}_{LL} + D^E{}_{LL}$.

Figures 9g-j display the radial diffusion coefficient (D_{LL}^B) of the 2MeV electrons and their radial diffusion time scale ($1/D_{LL}^B$) driven by the ULF waves at the two satellite locations. The red dashed lines (in Figures 9i and 9j) denote the empirical radial diffusion time scale ($1/(D^B{}_{LL} + D^E{}_{LL})$) for the 2MeV electrons at 90° pitch angle. After the dynamic pressure enhancement (after ~ 15:38UT), the outward radial diffusion coefficient (D_{LL}^B or D_{LL}) of the electrons increases with the increased K_p

(corresponding to the enhanced magnetic field fluctuation). Although the ULF waves can transport relativistic electrons at all pitch angles, the fastest radial diffusion time ($1/D_{LL}^{B}$) of the electrons is about ~7 days in the quasi-perpendicular direction (α~ 30°-150°) during the initial compression stage (15:38-16:00UT). Even though the electric field fluctuation is also involved into the electron radial diffusions, the time scale of the electron outward radial diffusions ($1/(D^{B}_{LL} + D^{E}_{LL})$) is also longer than 1 day in this event (The maximum K_p is 3 during the SSC, as indicated by Figure 1b). Although the outward radial diffusions have also some contributions to the electron loss during the SSC, the electron radial diffusion driven by ULF waves is slower than their pitch angle scatterings by the hiss and EMIC waves.

5. Summary and Conclusions

During the SSC from 31 October to 01 November 2012, two satellites of Van Allen Probes (RBSP-A/B) observed the relativistic electron loss associated with various waves outside the heart of outer radiation belt ($L^* \geq 5$). The relativistic electron loss mainly occurs in the field-aligned direction (pitch angle $\alpha < 30°$ or >150°), and the flux decay of the field-aligned electrons is independent of the spatial location variations of the two satellites. However, the relativistic electrons in the pitch angle range of 30°-150° increase (decrease) with the decreasing (increasing) geocentric distance ($|\Delta L| < 0.25$) of the RBSP-B (RBSP-A) location, and the electron fluxes in the quasi-perpendicular direction display energy-dispersive oscillations in the Pc5 period range (2 - 10min).

393 The relativistic electron loss is confirmed by the decrease of electron phase space
394 density at high-L shell after the magnetospheric compressions, and their loss is
395 associated with the intense plasmaspheric hiss, EMIC waves, relativistic electron
396 precipitation (observed by POES/NOAA satellites at ~ 850km) and magnetic field
397 fluctuations in the Pc5 band. The intense EMIC waves and whistler-mode hiss jointly
398 cause the rapidly pitch angle scattering loss of the relativistic electrons within 10
399 hours. Moreover, the Pc5 ULF waves also lead to the slowly outward radial diffusion
400 of the relativistic electrons in the high-L region with a negative electron phase space
401 density gradient. These results demonstrate that the relativistic electrons outside the
402 heart of outer radiation belt can undergo multiple losses during a SSC when various
403 waves are amplified prior to the storm main phase.
404
405 **Acknowledgments.** This work is supported by NSFC (41374165, 41431071).
406 Work by the RBSP-ECT team was supported by funding provided by
407 JHU/APL Contract No. 967399 under NASA's Prime Contract No. NAS5-01072.
408 RBSP data are available at the Web http://www.rbsp-ect.lanl.gov/data_pub/ and
409 https://emfisis.physics.uiowa.edu/. Solar wind and geomagnetic indices (P_d and H_{SYM})
410 and GOES13-14 data are available at the Web http://cdaweb.gsfc.nasa.gov/sp_phys
411 and http://satdat.ngdc.noaa.gov/sem/goes/data/. NOAA-POES data are available at the
412 web http://satdat.ngdc.noaa.gov/sem/poes/data. Authors thank the relevant staffs for
413 all data used in this paper. We also thank W. Liu for helpful discussion.
414

415 **Reference**

416 Baker, D. N., et al. (2012), The Relativistic Electron-Proton Telescope (REPT)
417 instrument on board the Radiation Belt Storm Probes (RBSP) spacecraft:
418 Characterization of Earth's radiation belt high-energy particle populations, *Space*
419 *Sci. Rev.*, doi:10.1007/s11214-012-9950-9.

420 Carson, B. R., C. J. Rodger, and M. A. Clilverd (2013), POES satellite observations of
421 EMIC-wave driven relativistic electron precipitation during 1998–2010, *J. Geophys.*
422 *Res. Let.*, 118, 232–243, doi:10.1029/2012JA017998.

423 Chen, Y., R. H. W. Friedel, G. D. Reeves, T. E. Cayton, and R. Christensen (2007),
424 Multisatellite determination of the relativistic electron phase space density at
425 geosynchronous orbit: An integrated investigation during geomagnetic storm times,
426 *J. Geophys. Res.*, 112, A11214, doi:10.1029/2007JA012314.

427 Claudepierre, S. G., et al. (2013), Van Allen Probes observation of localized drift
428 resonance between poloidal mode ultra-low frequency waves and 60 keV electrons,
429 Geophys. Res. Lett., 40, 4491–4497, doi:10.1002/grl.50901.

430 Clausen, L. B. N., J. B. H. Baker, J. M. Ruohoniemi, and H. J. Singer (2011), EMIC
431 waves observed at geosynchronous orbit during solar minimum: Statistics and
432 excitation, *J. Geophys. Res.*, 116, A10205, doi:10.1029/2011JA016823.

433 Evans, D. S., and M. S. Greer (2000), *Polar Orbiting Environmental Satellite Space*
434 *Environment Monitor 2: Instrument Description and Archive Data Documentation*,
435 NOAA Tech. Memo. OAR SEC-93, NOAA, Boulder, Colo.

436 Fei, Y., A. A. Chan, S. R. Elkington, and M. J. Wiltberger (2006), Radial diffusion and

MHD particle simulations of relativistic electron transport by ULF waves in the September 1998 storm, *J. Geophys. Res.*, 111, A12209, doi:10.1029/2005JA011211.

Hudson, M. K., D. N. Baker, J. Goldstein, B. T. Kress, J. Paral, F. R. Toffoletto, and M. Wiltberger (2014), Simulated magnetopause losses and Van Allen Probe flux dropouts, *Geophys. Res. Lett.*, 41, doi:10.1002/2014GL059222.

Kim, H. - J., and A. Chan (1997), Fully adiabatic changes in storm time relativistic electron fluxes, *J. Geophys. Res.*, 102, 22,107–22,116.

Kim, K. C., D.-Y. Lee, H.-J. Kim, L. R. Lyons, E. S. Lee, M. K. Öztürk, and C. R. Choi (2008), Numerical calculations of relativistic electron drift loss effect, *J. Geophys. Res.*, 113, A09212, doi:10.1029/2007JA013011.

Kletzing et al. (2013), The Electric and Magnetic Field Instrument Suite and Integrated Science (EMFISIS) on RBSP, *Space Sci. Rev.*, doi:10.1007/s11214-013-9993-6.

Kurth, W. S., S. De Pascuale, J. B. Faden, C. A. Kletzing, G. B. Hospodarsky, S. Thaller, and J. R. Wygant (2015), Electron densities inferred from plasma wave spectra obtained by the Waves instrument on Van Allen Probes, *J. Geophys. Res. Space Physics*, 120, 904–914, doi:10.1002/2014JA020857.

Lee, D.-Y., L. R. Lyons, and G. D. Reeves (2005), Comparison of geosynchronous energetic particle flux responses to solar wind dynamic pressure enhancements and substorms, *J. Geophys. Res.*, 110, A09213, doi:10.1029/2005JA011091.

458 Li, L. Y., J. B. Cao, G. C. Zhou, and X. Li (2009), Statistical roles of storms and
459 substorms in changing the entire outer zone relativistic electron population, *J.*
460 *Geophys. Res.*, 114, A12214, doi:10.1029/2009JA014333.
461 Li, L. Y., J. B. Cao, J. Y. Yang, and Y. X. Dong (2013a), Joint responses of
462 geosynchronous magnetic field and relativistic electrons to external changes in
463 solar wind dynamic pressure and interplanetary magnetic field, *J. Geophys. Res.*
464 *Space Physics*, 118, 1472–1482, doi:10.1002/jgra.50201.
465 Li, L. Y., J. Yu, J. B. Cao, D. Zhang, X. H. Wei, Z. J. Rong, J. Y. Yang, and H. S. Fu
466 (2013b), Rapid loss of the plasma sheet energetic electrons associated with the
467 growth of whistler mode waves inside the bursty bulk flows, *J. Geophys. Res.*
468 *Space Physics*, 118, 7200–7210, doi:10.1002/2013JA019109.
469 Li, W., Y. Y. Shprits, and R. M. Thorne (2007), Dynamic evolution of energetic outer
470 zone electrons due to wave-particle interactions during storms, *J. Geophys.*
471 *Res.*,112, A10220, doi:10.1029/2007JA012368.
472 Li, W., Q. Ma, R. M. Thorne, J. Bortnik, C.A.Kletzing,W. S. Kurth,G.
473 B.Hospodarsky, and Y. Nishimura (2015), Statistical properties of plasmaspheric
474 hiss derived from Van Allen Probes data and their Effects on radiation belt electron
475 dynamics, *J. Geophys. Res. Space Physics*, 120, doi:10.1002/2015JA021048.
476 Liu, W., T. E. Sarris, X. Li, S. R. Elkington, R. Ergun, V. Angleopoulos, J. Bonnell,
477 and K. H. Glassmeier (2009), Electric and magnetic field observations of Pc4 and
478 Pc5 pulsations in the inner magnetosphere: A statistical study, *J. Geophys. Res.*,
479 114, A12206, doi:10.1029/2009JA014243.

480 Li, X., I. Roth, M. Temerin, J.Wygant, M. K. Hudson, and J. B. Blake (1993),
481 Simulation of the prompt energization and transport of radiation particles during
482 the March 23, 1991 SSC, *Geophys. Res. Lett.*, 20, 2423 – 2426,
483 doi:10.1029/93GL02701.
484 Li, X. L., D. N. Baker, S. Elkington, M. Temerin, G. D. Reeves, R. D. Belian, J. B.
485 Blake, H. J. Singer, W. Peria, and G. Parks (2003), Energetic particle injections in
486 the inner magnetosphere as a response to an interplanetary shock, *J. Atmos. Sol.*
487 *Terr. Phys.*, 65, 233–244.
488 Loto'aniu, T. M., H. J. Singer, C. L. Waters, V. Angleopoulos, I. R. Mann, S. R.
489 Elkington, and J. W. Bonnell (2010), Relativistic electron loss due to ultralow
490 frequency waves and enhanced outward radial diffusion, *J. Geophys. Res.*, 115,
491 A12245,doi:10.1029/2010JA015755.
492 Lyons, L. R., and D. J. Williams (1984), *Quantitative Aspects of Magnetospheric*
493 *Physics*, Springer, New York.
494 Mann, I. R., et al. (2008), The upgraded CARISMA magnetometer array in the
495 THEMIS era, *Space Sci. Rev.*, 141, 413–451.
496 Mann, I. R. et al. Discovery of the action of a geophysical synchrotron in the Earth's
497 Van Allen radiation belts. *Nat. Commun*. 4:2795 doi: 10.1038/ncomms3795 (2013).
498 Matsumura, C., Y. Miyoshi, K. Seki, S. Saito, V. Angleopoulos, and J. Koller (2011),
499 Outer radiation belt boundary location relative to the magnetopause: Implications
500 for magnetopause shadowing, *J. Geophys. Res.*, 116, A06212,
501 doi:10.1029/2011JA016575.

502 Meredith, N. P., R. M. Thorne, R. B. Horne, D. Summers, B. J. Fraser, and R. R.
503 Anderson (2003), Statistical analysis of relativistic electron energies for cyclotron
504 resonance with EMIC waves observed on CRRES, *J. Geophys. Res.*, 108(A6), 1250,
505 doi:10.1029/2002JA009700.
506 Min, K., J. Lee, K. Keika, and W. Li (2012), Global distribution of EMIC waves
507 derived from THEMIS observations, *J. Geophys. Res.*, 117, A05219,
508 doi:10.1029/2012JA017515.
509 Morley, S. K., M. G. Henderson, G. D. Reeves, R. H. W. Friedel, and D. N. Baker
510 (2013), Phase Space Density matching of relativistic electrons using the Van Allen
511 Probes: REPT results, *Geophys. Res. Lett.*, *40*, 4798–4802, doi:10.1002/grl.50909.
512 Ni, B., J. Bortnik, R. M. Thorne, Q. Ma, and L. Chen (2013), Resonant scattering and
513 resultant pitch angle evolution of relativistic electrons by plasmaspheric hiss, *J.*
514 *Geophys. Res. Space Physics*, 118, 7740–7751, doi:10.1002/2013JA019260.
515 Ozeke, L. G., I. R. Mann, K. R. Murphy, I. Jonathan Rae, and D. K. Milling (2014),
516 Analytic expressions for ULF wave radiation belt radial diffusion coefficients, *J.*
517 *Geophys. Res. Space Physics*, 119, 1587-1605, doi:10.1002/2013JA019204.
518 Reeves, G. D., K. L. McAdams, R. H. W. Friedel, and T. P. O'Brien (2003),
519 Acceleration and loss of relativistic electrons during geomagnetic storms, *Geophys.*
520 *Res. Lett.*, 30(10), 1529, doi:10.1029/2002GL016513.
521 Reeves, G. D., et al. (2013), Electron acceleration in the heart of the Van Allen
522 radiation belts, *Science*, 341, 991–994, doi:10.1126/science.1237743.

523 Saito, S., Y. Miyoshi, and K. Seki (2010), A split in the outer radiation belt by
524 magnetopause shadowing: Test particle simulations, *J. Geophys. Res.*, 115, A08210,
525 doi:10.1029/2009JA014738.
526 Santolík, O., M. Parrot, and F. Lefeuvre, Singular value decomposition methods for
527 wave propagation analysis, *Radio Sci.*, 38(1), 1010, doi:10.1029/2000RS002523,
528 2003.
529 Sheeley, B. W., M. B. Moldwin, H. K. Rassoul, and R. R. Anderson (2001), An
530 empirical plasmasphere and trough density model: CRRES observations, *J.*
531 *Geophys. Res.*, 106, 25,631.
532 Shprits, Y. Y., R. M. Thorne, R. H. W. Friedel, G. D. Reeves, J. Fennell, D. N. Baker,
533 and S. G. Kanekal (2006), Outward radial diffusion driven by losses at
534 magnetopause, *J. Geophys. Res.*, 111, A11214, doi:10.1029/2006JA011657.
535 Shprits, Y. Y., L. Chen, and R. M. Thorne (2009), Simulations of pitch angle
536 scattering of relativistic electrons with MLTdependent diffusion coefficients, *J.*
537 *Geophys*. *Res*., 114, A03219, doi:10.1029/2008JA013695.
538 Shue, J.-H., et al. (1998), Magnetopause location under extreme solar wind conditions,
539 J. Geophys. Res., 103(A8), 17,691–17,700, doi:10.1029/98JA01103.
540 Stix, T. H. (1992), *Waves in Plasmas*, Am. Inst. of Phys., New York.
541 Spence, H. E., et al. (2013), Science Goals and Overview of the Energetic Particle,
542 Composition, and Thermal Plasma (ECT) Suite on NASA's Radiation Belt Storm
543 Probes (RBSP) Mission, *Space Sci. Rev.*, doi: 10.1007/s11214-013-0007-5.

544 Su, Z., H. Zhu, F. Xiao, H. Zheng, C. Shen, Y. Wang, and S. Wang (2012),
545 Bounce-averaged advection and diffusion coefficients for monochromatic
546 electromagnetic ion cyclotron wave: Comparison between test-particle and
547 quasi-linear models, *J. Geophys. Res.*, 117, A09222, doi:10.1029/2012JA017917.
548 Summers, D., and R. M. Thorne (2003), Relativistic electron pitch-angle scattering by
549 electromagnetic ion cyclotron waves during geomagnetic storms, *J. Geophys. Res.*,
550 108(A4), 1143, doi:10.1029/2002JA009489.
551 Summers, D. (2005), Quasi-linear diffusion coefficients for field-aligned
552 electromagnetic waves with applications to the magnetosphere, J. Geophys. Res.,
553 110, A08213, doi:10.1029/2005JA011159.
554 Summers, D., B. Ni, and N. P. Meredith (2007), Timescales for radiation belt electron
555 acceleration and loss due to resonant wave-particle interactions: 2. Evaluation for
556 VLF chorus, ELF hiss, and electromagnetic ion cyclotron waves, *J. Geophys. Res.*,
557 112, A04207, doi:10.1029/2006JA011993
558 Thorne, R. M. (2010), Radiation belt dynamics: The importance of wave-particle
559 interactions, *Geophys. Res. Lett.*, 37, L22107, doi:10.1029/2010GL044990.
560 Tsyganenko, N. A. (1989), A magnetospheric magnetic field model with a warped tail
561 current sheet, *Planet. Space Sci.*, *37*, 5–20, doi:10.1016/0032-0633(89)90066-4.
562 Tsyganenko, N. A., and M. I. Sitnov (2005), Modeling the dynamics of the inner 542
563 magnetosphere during strong geomagnetic storms, *J. Geophys. Res.*, 110, A03208,
564 543 doi:10.1029/2004JA010798.
565 Tu, W., S. R. Elkington, X. Li, W. Liu, and J. Bonnell (2012), Quantifying radial

566 diffusion coefficients of radiation belt electrons based on global MHD simulation
567 and spacecraft measurements, *J. Geophys. Res.*, 117, A10210,
568 doi:10.1029/2012JA017901
569 Tu, W., G. S. Cunningham, Y. Chen, M. 417 G. Henderson, E. Camporeale, and G. D.
570 Reeves (2013), Modeling radiation belt electron dynamics during GEM challenge
571 intervals with the DREAM3D diffusion model, *J. Geophys. Res. Space Physics*,
572 118, 6197–6211, doi:10.1002/jgra.50560.
573 Turner, D. L., Y. Shprits, M. Hartinger, and V. Angleopoulos (2012), Explaining
574 sudden losses of outer radiation belt electrons during geomagnetic storms, *Nat.*
575 *Phys*., 8(3), 208–212, doi:10.1038/nphys2185.
576 Turner, D. L., V. Angleopoulos, W. Li, M. D. Hartinger, M. Usanova, I. R. Mann, J.
577 Bortnik, and Y. Shprits (2013), On the storm-time evolution of relativistic electron
578 phase space density in Earth's outer radiation belt, *J. Geophys. Res. Space Physics,*
579 *118*, 2196–2212, doi:10.1002/jgra.50151.
580 Usanova, M. E., et al. (2014), Effect of EMIC waves on relativistic and
581 ultra-relativistic electron populations: Ground-based and Van Allen Probes
582 Observations, *Geophys. Res. Lett.*, doi:10.1002/2013GL059024.
583 Wang, Z., Z. Yuan, M. Li, H. Li, D. Wang, H. Li, S. Huang, and Z. Qiao (2014),
584 Statistical characteristics of EMIC wave-driven relativistic electron precipitation
585 with observations of POES satellites: Revisit, *J. Geophys. Res. Space Physics*, 119,
586 5509–5519, doi:10.1002/2014JA020082.
587 Xiao, F., Z. Su, H. Zheng, and S. Wang (2009), Modeling of outer radiation belt

588 electrons by multidimensional diffusion process, *J. Geophys. Res.*, 114, A03201,
589 doi:10.1029/2008JA013580.
590 Yuan, Z., M. Li, Y. Xiong, H. Li, M. Zhou, D. Wang, S. Huang, X. Deng, and J. Wang
591 (2013), Simultaneous observations of precipitating radiation belt electrons and ring
592 current ions associated with the plasmaspheric plume, *J. Geophys. Res. Space*
593 *Physics*, 118, 4391–4399, doi:10.1002/jgra.50432.
594

595 **Captions**

596 Figure 1. Relativistic electron loss (in the red rectangle) observed by RBSP-B satellite
597 during the late stage of a SSC from 30 October to 01 November 2012. (a) Solar wind
598 dynamic pressure (P_d) and subsolar magnetopause position (R_{MP}). (b) H-component of
599 geomagnetic field (H_{SYM}) and K_p index. (c) Energy spectra of relativistic electrons
600 measured by the REPT instrument on board the RBSP-B. (d) L value of the satellite
601 location. The similar electron flux change is also observed by the RBSP-A satellite.
602

603 Figure 2. (a-b) Radial (L*) profile of the relativistic electron phase space density
604 observed by the RBSP-B in different intervals. Different times correspond to the start
605 time of each pass. The electron adiabatic invariants (μ, K, L^*) and phase space density
606 (f) are calculated through the REPT electron data and TS04D magnetic field model
607 [*Tsyganenko and Sitnov*, 2005]. (c) Observed value (colored asterisks) of magnetic
608 field versus the TS04D model value. (d) Occurrence probability of relative error
609 $((B_{observed}-B_{model})/B_{observed})$ during the SSC.

610

611 Figure 3. (a, b) Observed value (black solid line) of magnetic field, TS04D model
612 value (black dash line), and relative error (($B_{observed}$-B_{model})/$B_{observed}$, red dot line). (c-n)
613 Spin-averaged fluxes (j_e) and pitch angle distributions of relativistic electrons.

614

615 Figure 4. Equatorial (L-MLT plane) projection of the wave observed locations during
616 the interval 15:30- 16:30 UT on 31 October 2012. Ground stations include the
617 MCMU, RABB, FSMI, OXFO, SOD, IVA and KIL. Satellites include the RBSP-A,
618 RBSP-B, GOES-13 and GOES-14. Particle precipitation location (i.e., the NOAA-16
619 location) is marked by purple line.

620

621 Figure 5. Power spectra density (PSD) of the EMIC waves observed by the GOES-13
622 and ground stations (MCMU, RABB, FSMI) on 31 October 2012.

623

624 Figure 6 (a) Plasma density, (b) Power spectral density (PSD) of magnetic field, (c)
625 Wave normal angle (WNA), and (d) Polarization ellipticity. Frequency range of
626 whistler-mode waves are from $0.01f_{ce}$ (dash line) to $0.5f_{ce}$ (dot line), and its WNA<
627 15°, and its ellipticity > 0.5.

628

629 Figure 7. (a-c) Bounced-drift-averaged pitch-angle diffusion coefficient $<D_{\alpha\alpha}>$. (d-f)
630 Pitch angle evolution of relativistic electrons driven by the hiss and EMIC waves. The
631 blue and red dots are the observed electron pitch angle distributions before and after

632 the magnetospheric compressions, respectively.

633

634 Figure 8. Fluxes of the trapped (90°) and precipitating (0°) particles measured by
635 LEO satellites at ~ 850km during the SSC (after 15:38UT on 31 October). The gray
636 shadowing denotes the precipitation of the energetic protons and MeV electrons.

637

638 Figure 9. (a-f) Power spectral density (PSD) of magnetic field in the radial, azimuthal
639 and field-aligned directions. (g-j) Radial diffusion coefficient (D_{LL}^{B}) of the 2MeV
640 electrons and their radial diffusion time scale ($1/D_{LL}^{B}$) driven by ULF waves at the two
641 satellite locations. The red dash lines (in Figures 9i, j) denote the empirical radial
642 diffusion time scale ($1/(D^{B}_{LL} + D^{E}_{LL})$) for the 2MeV electrons at 90° pitch angle
643 [*Ozeke et al.*, 2014].

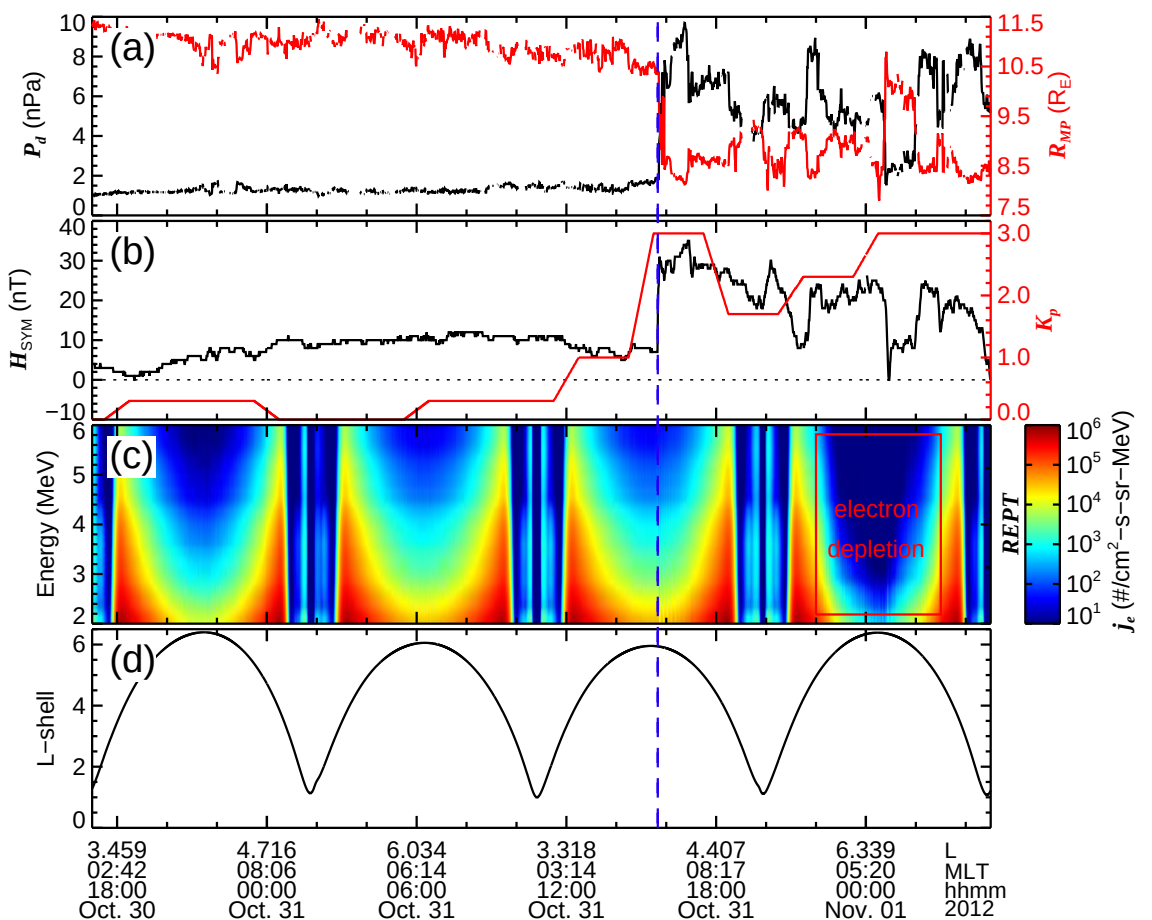
(a)
P_d (nPa)
R_{MP} (R_E)
(b)
H_{SYM} (nT)
K_p
(c)
Energy (MeV)
electron
depletion
REPT
j_e (#/cm^2−s−sr−MeV)
(d)
L−shell
3.459
02:42
18:00
Oct. 30
4.716
08:06
00:00
Oct. 31
6.034
06:14
06:00
Oct. 31
3.318
03:14
12:00
Oct. 31
4.407
08:17
18:00
Oct. 31
6.339
05:20
00:00
Nov. 01
L
MLT
hhmm
2012

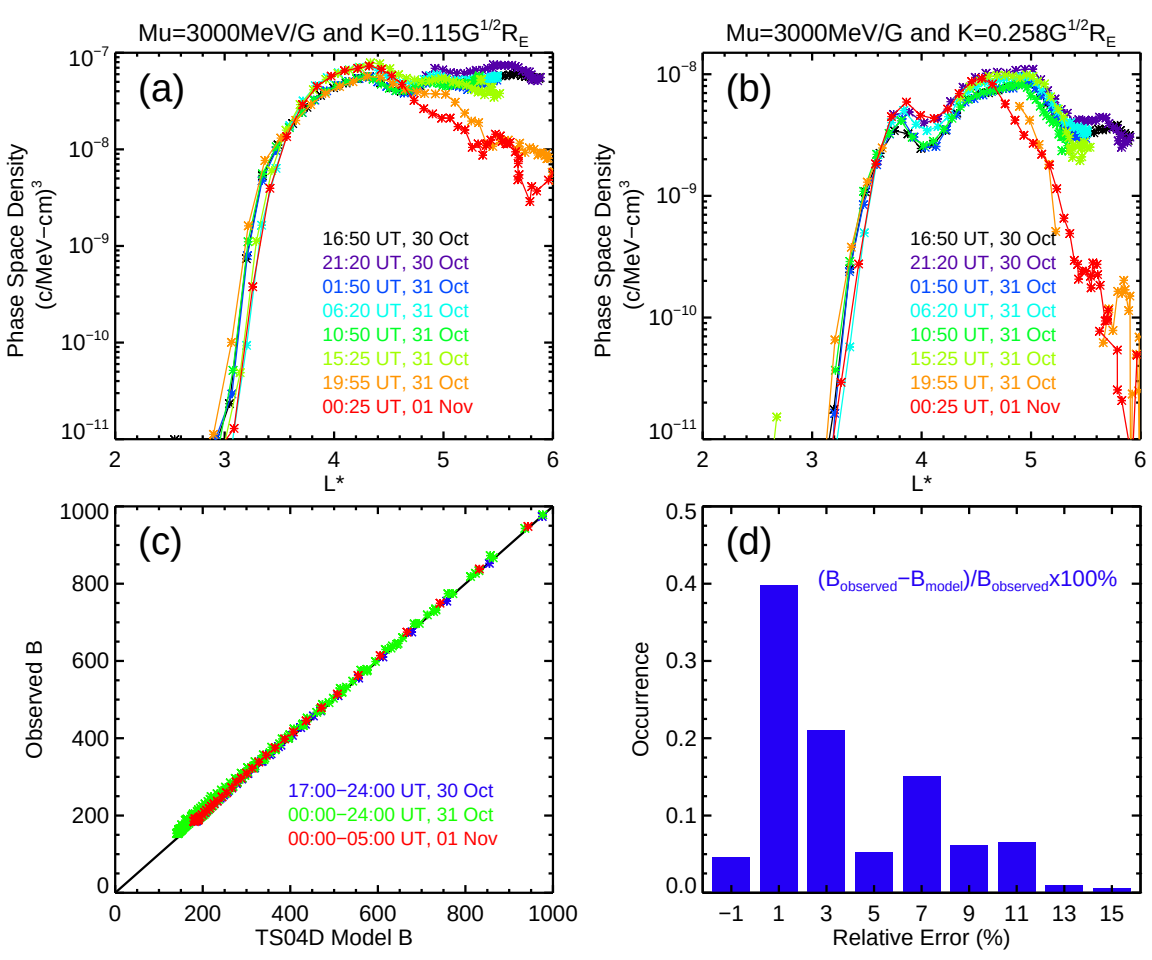
Mu=3000MeV/G and K=0.115G^1/2R_E
(a)
Phase Space Density (c/MeV−cm)^3
L*
16:50 UT, 30 Oct
21:20 UT, 30 Oct
01:50 UT, 31 Oct
06:20 UT, 31 Oct
10:50 UT, 31 Oct
15:25 UT, 31 Oct
19:55 UT, 31 Oct
00:25 UT, 01 Nov
Mu=3000MeV/G and K=0.258G^1/2R_E
(b)
Phase Space Density (c/MeV−cm)^3
L*
16:50 UT, 30 Oct
21:20 UT, 30 Oct
01:50 UT, 31 Oct
06:20 UT, 31 Oct
10:50 UT, 31 Oct
15:25 UT, 31 Oct
19:55 UT, 31 Oct
00:25 UT, 01 Nov
(c)
Observed B
TS04D Model B
17:00−24:00 UT, 30 Oct
00:00−24:00 UT, 31 Oct
00:00−05:00 UT, 01 Nov
(d)
(B_observed−B_model)/B_observedx100%
Occurrence
Relative Error (%)

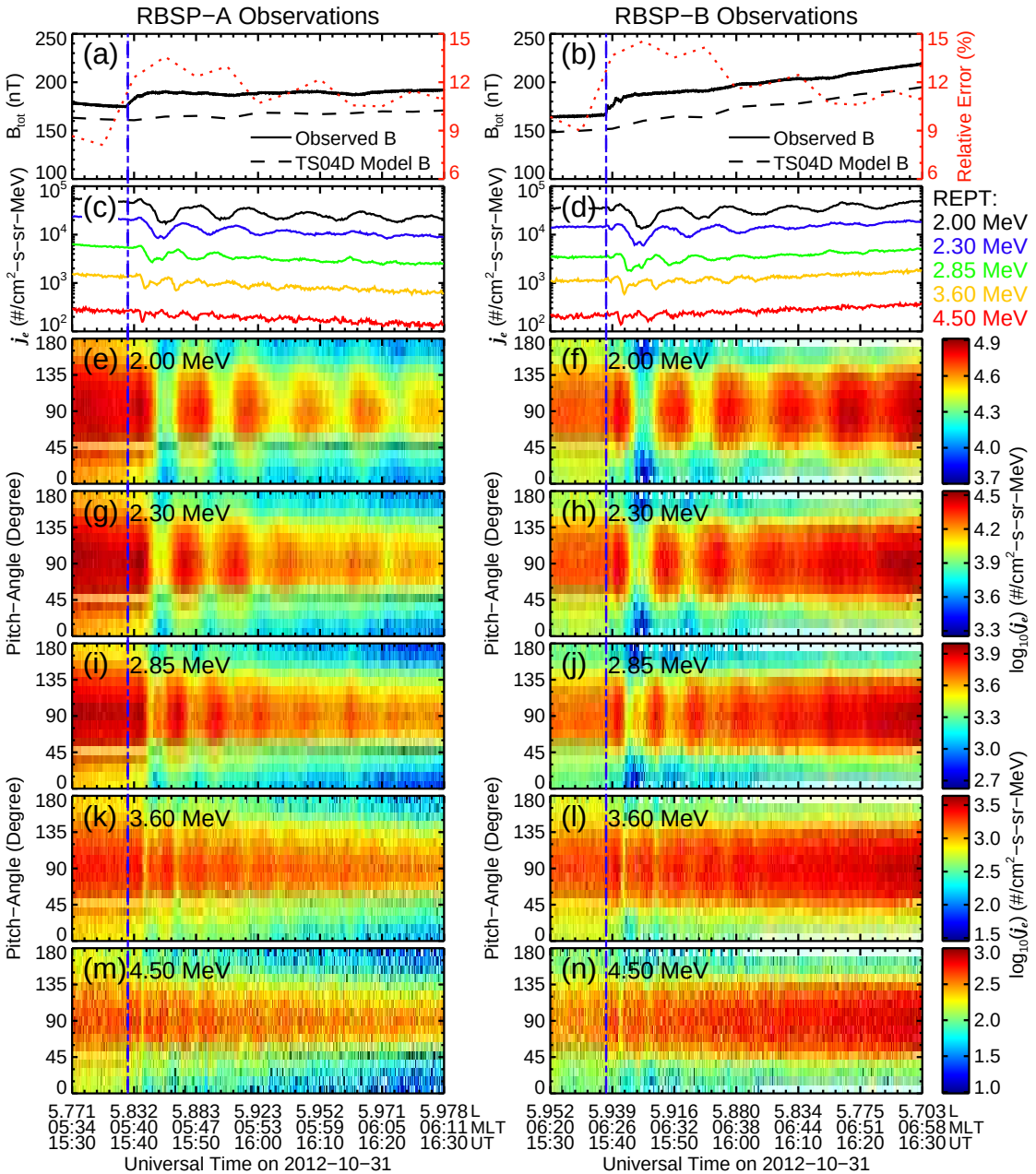
RBSP−A Observations
RBSP−B Observations
(a)
(b)
(c)
(d)
(e) 2.00 MeV
(f) 2.00 MeV
(g) 2.30 MeV
(h) 2.30 MeV
(i) 2.85 MeV
(j) 2.85 MeV
(k) 3.60 MeV
(l) 3.60 MeV
(m) 4.50 MeV
(n) 4.50 MeV
B_tot (nT)
Relative Error (%)
Observed B
TS04D Model B
j_e (#/cm²−s−sr−MeV)
REPT:
2.00 MeV
2.30 MeV
2.85 MeV
3.60 MeV
4.50 MeV
Pitch−Angle (Degree)
log10(J_e) (#/cm²−s−sr−MeV)
5.771 5.832 5.883 5.923 5.952 5.971 5.978 L
05:34 05:40 05:47 05:53 05:59 06:05 06:11 MLT
15:30 15:40 15:50 16:00 16:10 16:20 16:30 UT
Universal Time on 2012−10−31
5.952 5.939 5.916 5.880 5.834 5.775 5.703 L
06:20 06:26 06:32 06:38 06:44 06:51 06:58 MLT
15:30 15:40 15:50 16:00 16:10 16:20 16:30 UT
Universal Time on 2012−10−31

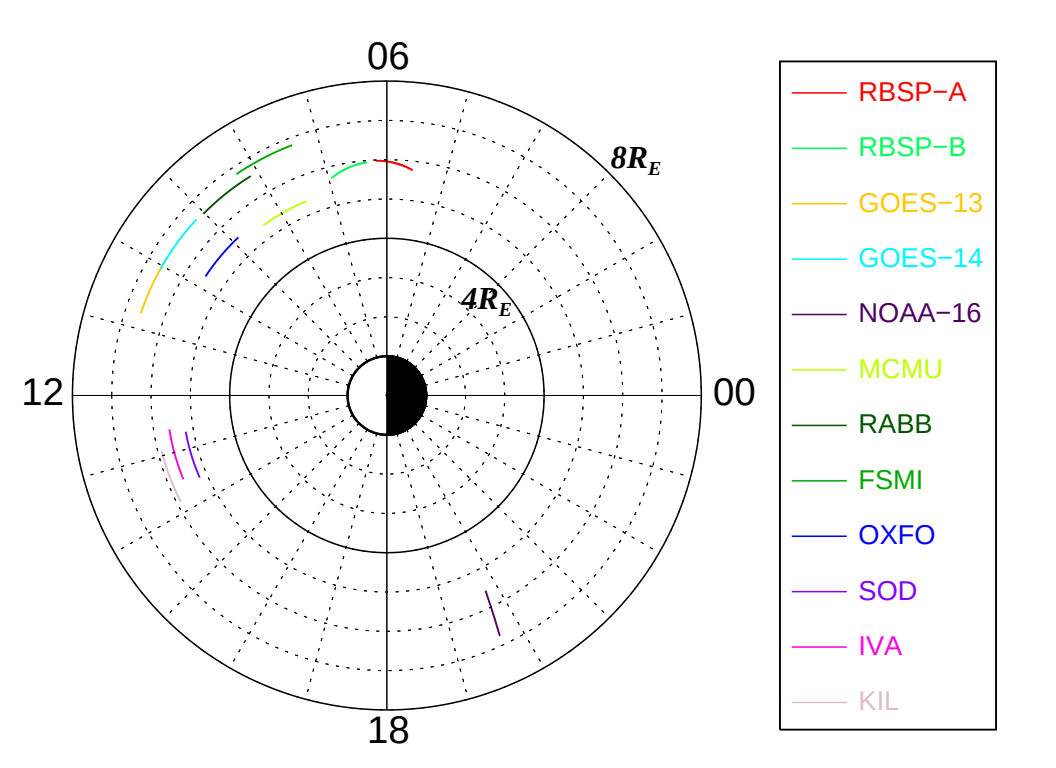
06
12
00
18
$8R_E$
$4R_E$
RBSP−A
RBSP−B
GOES−13
GOES−14
NOAA−16
MCMU
RABB
FSMI
OXFO
SOD
IVA
KIL

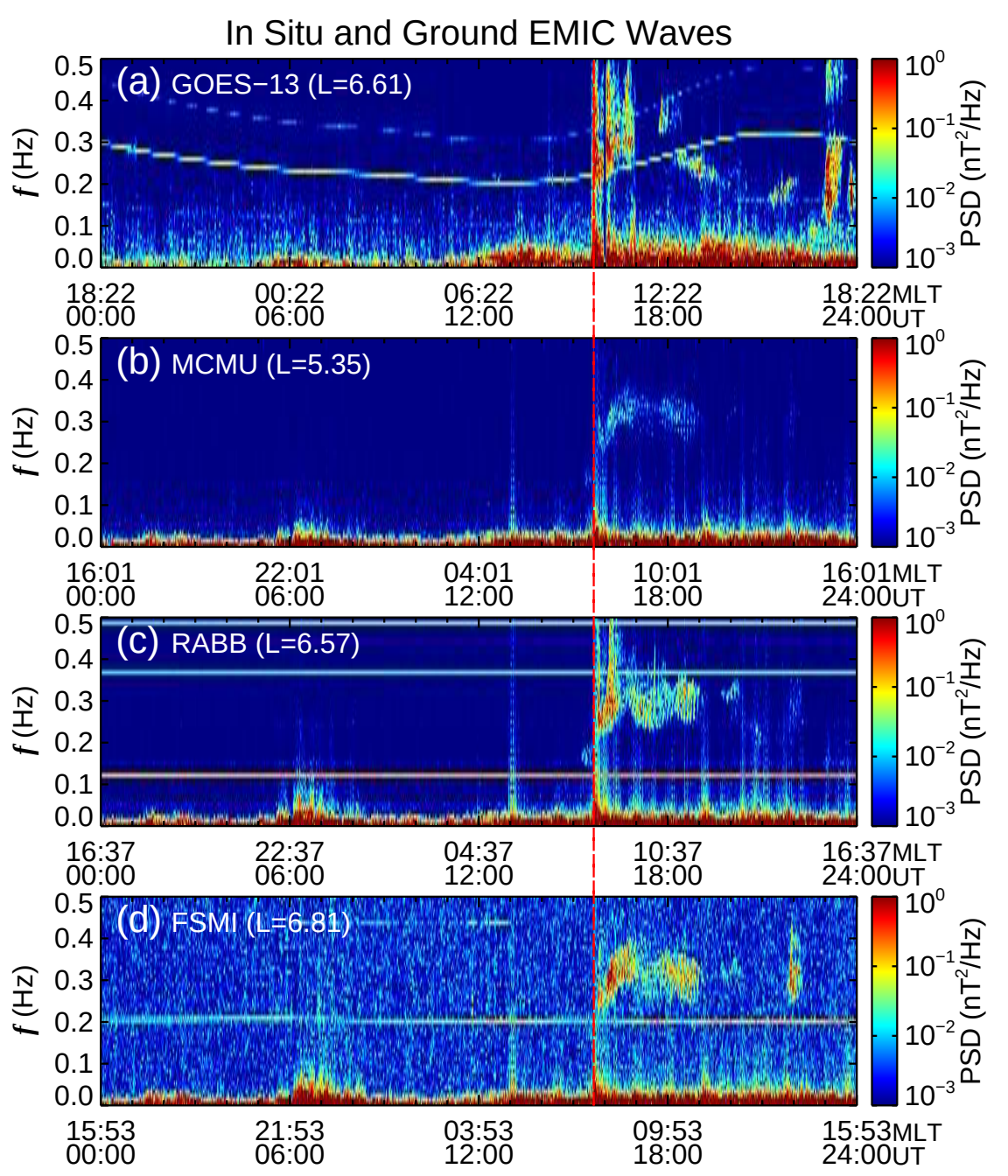
In Situ and Ground EMIC Waves
(a) GOES−13 (L=6.61)
(b) MCMU (L=5.35)
(c) RABB (L=6.57)
(d) FSMI (L=6.81)
f (Hz)
0.5
0.4
0.3
0.2
0.1
0.0
PSD (nT²/Hz)
10⁰
10⁻¹
10⁻²
10⁻³
18:22 00:00 06:22 12:22 18:22 MLT
00:22 06:00 12:00 18:00 24:00 UT
16:01 22:01 04:01 10:01 16:01 MLT
00:00 06:00 12:00 18:00 24:00 UT
16:37 22:37 04:37 10:37 16:37 MLT
00:00 06:00 12:00 18:00 24:00 UT
15:53 21:53 03:53 09:53 15:53 MLT
00:00 06:00 12:00 18:00 24:00 UT

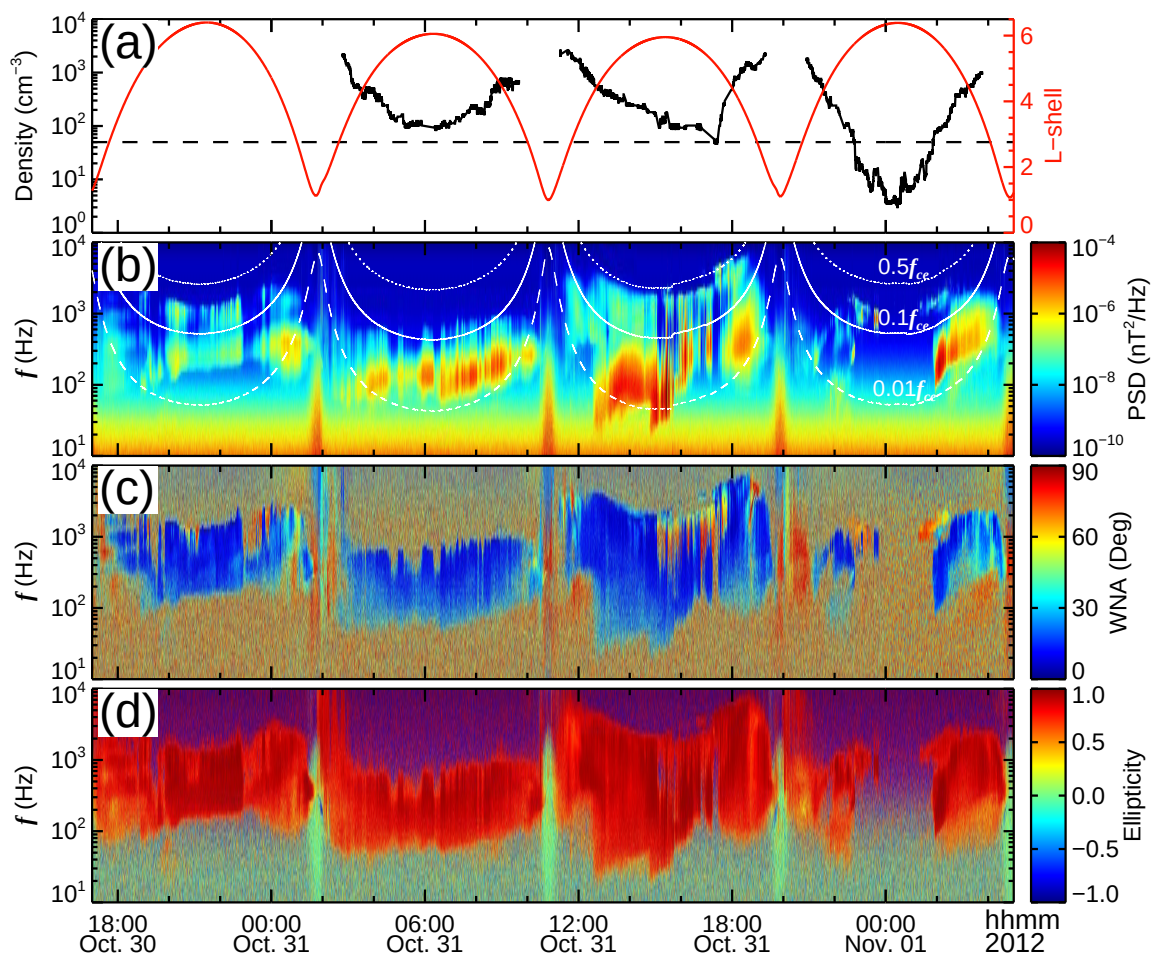
(a)
Density (cm^{-3})
L–shell
(b)
f (Hz)
$0.5f_{ce}$
$0.1f_{ce}$
$0.01f_{ce}$
PSD (nT^2/Hz)
(c)
WNA (Deg)
(d)
Ellipticity
18:00 Oct. 30
00:00 Oct. 31
06:00 Oct. 31
12:00 Oct. 31
18:00 Oct. 31
00:00 Nov. 01
hhmm 2012

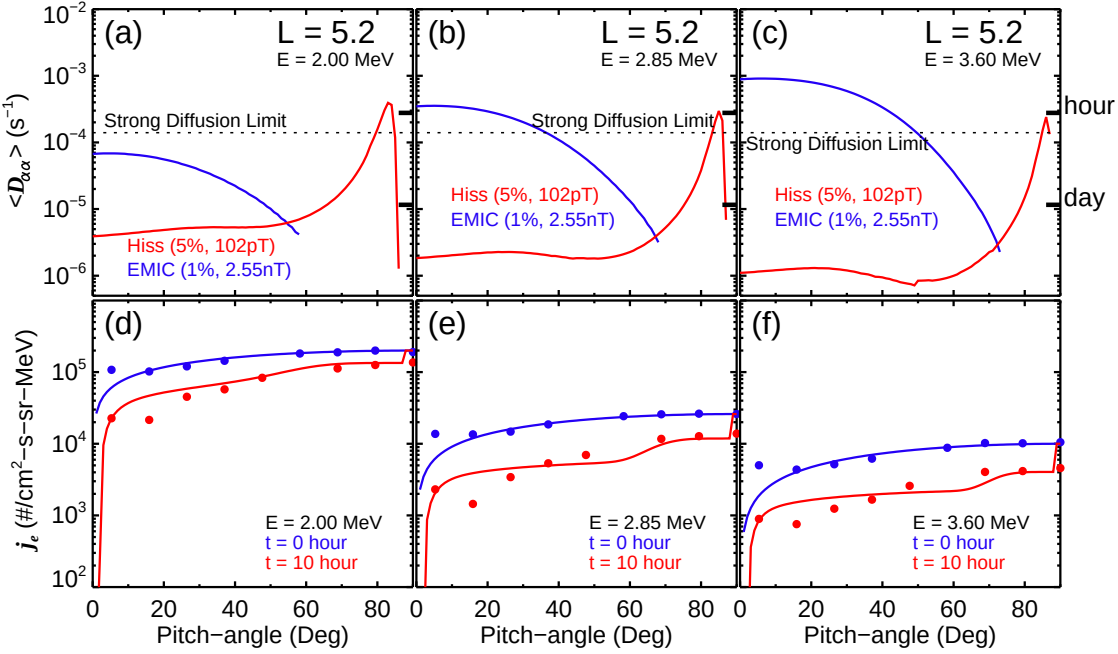
(a)
L = 5.2
E = 2.00 MeV
Strong Diffusion Limit
Hiss (5%, 102pT)
EMIC (1%, 2.55nT)
(b)
L = 5.2
E = 2.85 MeV
Strong Diffusion Limit
Hiss (5%, 102pT)
EMIC (1%, 2.55nT)
(c)
L = 5.2
E = 3.60 MeV
Strong Diffusion Limit
Hiss (5%, 102pT)
EMIC (1%, 2.55nT)
hour
day
<Dαα> (s−1)
(d)
(e)
(f)
je (#/cm2−s−sr−MeV)
E = 2.00 MeV
t = 0 hour
t = 10 hour
E = 2.85 MeV
t = 0 hour
t = 10 hour
E = 3.60 MeV
t = 0 hour
t = 10 hour
Pitch−angle (Deg)
Pitch−angle (Deg)
Pitch−angle (Deg)

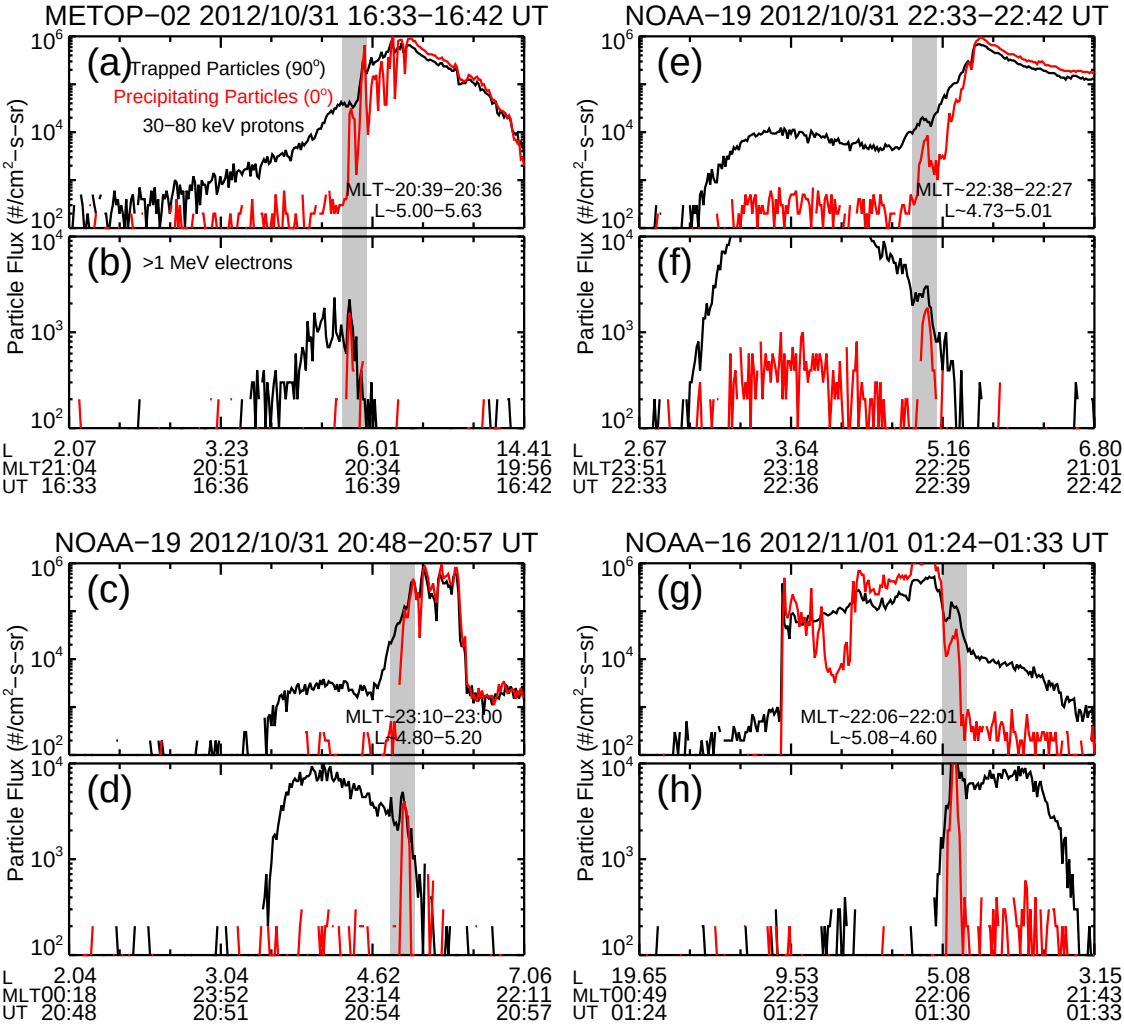
METOP−02 2012/10/31 16:33−16:42 UT
(a)
Trapped Particles (90°)
Precipitating Particles (0°)
30−80 keV protons
MLT~20:39−20:36
L~5.00−5.63
(b)
>1 MeV electrons
Particle Flux (#/cm²−s−sr)
L 2.07 3.23 6.01 14.41
MLT 21:04 20:51 20:34 19:56
UT 16:33 16:36 16:39 16:42
NOAA−19 2012/10/31 22:33−22:42 UT
(e)
MLT~22:38−22:27
L~4.73−5.01
(f)
L 2.67 3.64 5.16 6.80
MLT 23:51 23:18 22:25 21:01
UT 22:33 22:36 22:39 22:42
NOAA−19 2012/10/31 20:48−20:57 UT
(c)
MLT~23:10−23:00
L~4.80−5.20
(d)
L 2.04 3.04 4.62 7.06
MLT 00:18 23:52 23:14 22:11
UT 20:48 20:51 20:54 20:57
NOAA−16 2012/11/01 01:24−01:33 UT
(g)
MLT~22:06−22:01
L~5.08−4.60
(h)
L 19.65 9.53 5.08 3.15
MLT 00:49 22:53 22:06 21:43
UT 01:24 01:27 01:30 01:33

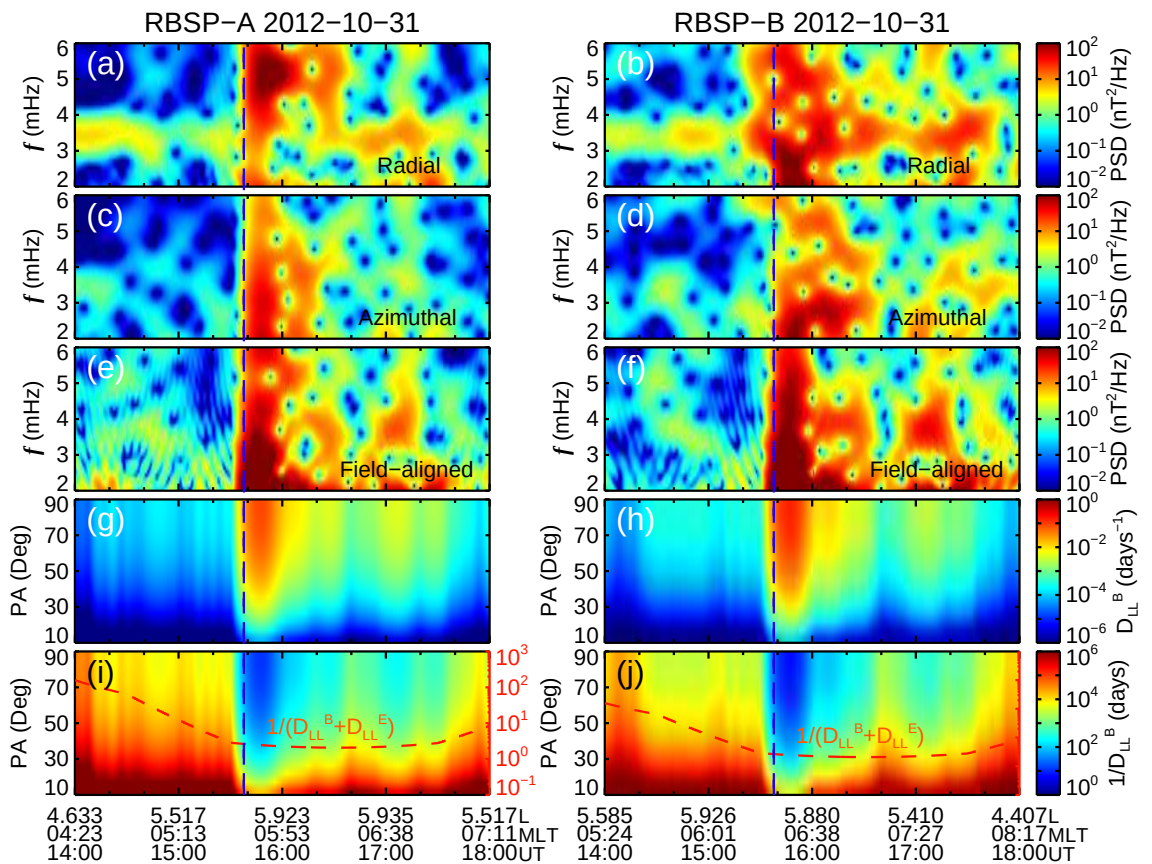
RBSP−A 2012−10−31
RBSP−B 2012−10−31
(a)
(b)
(c)
(d)
(e)
(f)
(g)
(h)
(i)
(j)
Radial
Azimuthal
Field−aligned
f (mHz)
PA (Deg)
PSD (nT²/Hz)
D_LL^B (days⁻¹)
1/D_LL^B (days)
1/(D_LL^B+D_LL^E)
4.633 04:23 14:00
5.517 05:13 15:00
5.923 05:53 16:00
5.935 06:38 17:00
5.517L 07:11MLT 18:00UT
5.585 05:24 14:00
5.926 06:01 15:00
5.880 06:38 16:00
5.410 07:27 17:00
4.407L 08:17MLT 18:00UT